Journal of Nuclear Medicine, published on December 21, 2021 as doi:10.2967/jnumed.121.262968

Efficient delay correction for total-body PET kinetic modeling using pulse timing methods

Elizabeth J. Li[1], Benjamin A. Spencer[1], Jeffrey P. Schmall[2], Yasser Abdelhafez[3], Ramsey D. Badawi[3,1], Guobao Wang[3], and Simon R. Cherry[1,3]

[1]Department of Biomedical Engineering, University of California Davis, Davis, California, USA.

[2]United Imaging Healthcare America, Inc., Houston, Texas, USA.

[3]Department of Radiology, UC Davis Health, Sacramento, California, USA.

First and corresponding author: Elizabeth Li, Department of Biomedical Engineering, 451 E. Health Sciences Drive, Davis, CA, 95616, Email: lzli@ucdavis.edu, Phone: 530-752-0626

Disclaimer: None.

Financial support: NIH grants R01 CA206187 and R35 CA197608

Word count: 5380

Running title: Leading edge method for delay correction

ABSTRACT

Quantitative kinetic modeling requires an input function (IF). A non-invasive image-derived IF (IDIF) can be obtained from dynamic PET images. However, a robust IDIF location, (e.g. aorta), may be far away from a tissue of interest, particularly in total-body PET, introducing a time delay between the IDIF and the tissue. The standard practice of joint estimation (JE) of delay, along with model fitting, is computationally expensive. To improve the efficiency of delay correction for total-body PET parametric imaging, this study investigates the use of pulse timing methods to estimate and correct for delay.

Methods: Simulation studies were performed with a range of delay values, frame lengths and noise levels, to test the tolerance of two pulse timing methods—leading edge (LE) and constant fraction discrimination (CFD) and their thresholds. The methods were then applied to data from 21 subjects (14 healthy volunteers, 7 cancer patients) that underwent 60-minute dynamic uEXPLORER total-body ^{18}F-FDG PET acquisitions. Region-of-interest (ROI) kinetic analysis and parametric images were generated to compare LE and JE methods of delay correction, as well as no delay correction.

Results: Simulations demonstrated that a 10% LE threshold resulted in biases and standard deviations at tolerable levels for all noise levels tested, with 2-second frames. Pooled ROI-based results (N = 154) showed strong agreement between LE (10% threshold) and JE methods in estimating delay (Pearson's r=0.96, P<1E-3), and kinetic parameters v_b (r=0.96, P<1E-3), K_i (r=1.00, P<1E-3), and K_1 (r=0.97, P<1E-3). When tissues with minimal delay were excluded from pooled analyses, there were reductions in v_b (69.4%) and K_1 (4.8%) when delay correction was not performed. Similar results were obtained for parametric images; additionally, lesion K_i

contrast was improved overall with LE and JE delay correction compared to no delay correction and Patlak analysis.

Conclusion: This study demonstrates the importance of delay correction in total-body PET. LE delay correction can be an efficient surrogate for JE, taking a fraction of the computational time, and allowing for rapid delay correction across $>10^6$ voxels in total-body PET datasets.

Key words: dynamic PET, input function, delay correction, total-body PET

INTRODUCTION

An input function (IF) is required for fully quantitative PET kinetic modeling and can be derived through arterial blood sampling (ABS) (*1*). However, ABS is invasive, technically challenging, and can introduce additional errors in the measured IF arrival time and bolus shape, which may result in biased kinetic parameter estimates when left uncorrected (*2–4*). An image-derived input function (IDIF) can be sampled from the images directly, reducing errors in arrival time and removing the external dispersion introduced by ABS. Still, the delay between the IF peak and arrival time at a tissue or voxel of interest must be considered.

The advent of high-efficiency, long axial field-of-view scanners, such as the uEXPLORER total-body PET system (*5,6*), presents the opportunity for high signal-to-noise total-body kinetic modeling. Short frames with high count statistics are possible, for improved estimation of parameters such as delay. Additionally, an IDIF can be derived from the larger vessels, where partial volume effects are reduced. However with total-body PET, delay correction becomes more important because the IDIF will be further from a tissue of interest than a more localized IDIF (e.g. carotid IDIF for grey matter) and incorrect delay estimates may lead to parameter bias (*2–4*). Different tissues will also have their own unique delay values, so delay correction must be performed for every voxel or regional time activity curve (TAC).

Common methods of delay correction include: (i) setting delay to a predetermined value (*2,7*), (ii) adjusting the IF based on an IDIF close to the tissue of interest (*2,8*), or (iii) jointly-estimating delay during the fitting process (*4,9,10*). However, the widely-used joint estimation (JE) method is costly in terms of computation time, especially for voxel-level total-body PET, because it involves nonlinear fitting of kinetic parameters for all possible delay values. Therefore, a much faster method for estimating bolus delay would be beneficial. Applications where voxel-

level parametric imaging is important include the detection/quantification of metastatic lesions, and disease processes that result in heterogenous tracer delivery and uptake within a tissue or organ.

Here, we draw our inspiration from pulse timing methods, including leading edge (LE) and the constant fraction discriminator (CFD) methods, that are used to efficiently determine the arrival time of electronic pulses from a radiation detector (*11*). In this work, LE and CFD pulse timing methods are applied to TACs rather than electronic pulses. Delay is defined as $t_d - t_0$, which is the difference between the arrival times of the bolus in the region chosen to define the IF, t_0, and of a tissue or voxel TAC determined using one of the pulse timing methods, t_d. Implementation of pulse timing methods would greatly reduce the computational burden of the fitting process for a given kinetic model, since the non-linear least-squares fitting process can be performed for a single delay value, as determined by these methods. While these methods are computationally efficient, the choice of parameters (LE trigger threshold, CFD attenuation values) can impact delay estimation. Therefore, we investigate the use of pulse timing methods for time delay estimation and correction for quantitative total-body kinetic modeling and parametric imaging.

MATERIALS AND METHODS

Simulations

Computer simulations of TAC data were developed to evaluate bias and standard deviation (s.d.) of delay estimation approaches. A high-temporal resolution IF (0.1-second sampling) representing a bolus of ^{18}F-FDG was generated based on the tri-exponential function proposed by Feng *et al*. (*12*,*13*). The IF was shifted by 100 randomly selected delay values between 0 and

50 s. Brain grey matter TACs were simulated based on these delayed IFs and typical kinetic parameters (v_b = 0.05, K_1 = 0.06 (mL/min/mL), k_2 = 0.07 (min^{-1}), and k_3 = 0.07 (min^{-1}), k_4 = 0 (min^{-1})) from Huisman et al., (*14*). For each delay value, 500 noisy realizations were generated using a commonly used time-changing Gaussian noise model (*15*) with a mean equal to the initial activity concentration in frame *m*, and standard deviation $S_c \cdot \delta_m$:

$$TAC_m \sim Gaussian(\overline{TAC_m}, S_c\delta_m), \quad \delta_m = \sqrt{\frac{\overline{TAC_m} \cdot \exp(\lambda \Delta t_m)}{\Delta t_m}}$$

where δ_m is dependent on the radioisotope decay constant λ, frame length Δt, and mean activity concentration $\overline{TAC_m}$ in frame *m*. The scale S_c was set to four noise levels of 0.03, 0.1, 0.2, and 0.3 to encompass TACs with different statistical quality. To mimic zero-mean noise present in measured TACs prior to bolus arrival, the activity concentration included in $\delta_m$was modified to have a mean of 0.5% of the maximum TAC activity:

$$TAC_{early,m} \sim Gaussian(0, S_c\delta_m), \quad \delta_m = \sqrt{\frac{0.005 \cdot \max(\overline{TAC}) \cdot \exp(\lambda \Delta t_m)}{\Delta t_m}}.$$

TACs were then re-binned to frame lengths of 1, 2, 5, and 10 s and used to assess the impact of framing on delay estimates. Supplemental Fig. 1A shows an example TAC with S_c equal to 0.1.

For the LE method (*11*), a trigger threshold is selected and the time at which the signal amplitude passes that threshold is recorded as the arrival time. LE thresholds were set across a wide range (2.5 to 50%) of the peak activity in the first 120 seconds. A 10% LE threshold is shown in Supplemental Fig. 1B. For the CFD method (*11*), the TACs were shifted in time by 2 seconds for shorter framing, or by 1 frame for frames >2 seconds. Attenuated and inverted versions of the TAC (attenuated to between 2.5 and 50% of the peak activity) were added to the shifted TAC and the resulting zero-crossing point marks the arrival time (Supplemental Fig. 1C).

LE and CFD-based estimates for each combination of delay value, frame length, noise level, and % peak activity were determined. Average bias and standard deviation of the LE and CFD delay estimates were determined by comparing the estimates with the ground truth. Based on the results of these simulations, only the LE method was subsequently applied on human data.

Human Data

Institutional Review Board approval and written informed consent was obtained for 14 healthy volunteers (6 male, 8 female, body mass index (BMI): 19.4-37.0 kg/m^2, 26-78 years) and 7 male subjects with genitourinary cancer (GUC) (BMI: 20.1-32.0 kg/m^2, 56-76 years). Subjects were injected with an average dose of 357.8 MBq FDG (range: 331.9-391.8) and underwent 60-minute dynamic studies on the uEXPLORER scanner (*16*). Images were reconstructed with vendor-provided TOF-OSEM software (20 subsets, 4 iterations, 150x150x486 image matrix size, 4 mm isotropic voxels) with corrections for attenuation, scatter, randoms, deadtime and decay (*17*). No point spread function modeling was applied. For generating parametric images, image data were smoothed using a composite image prior and the kernel method (*18*). The following framing protocol was used to generate 66 timepoints: 30x2 s, 12x10 s, 6x30 s, 12x120 s, 6x300 s.

For all human data, an IDIF was derived from a region of interest (ROI) in the left ventricle. Tissue compartment model selection was incorporated to account for tissue spaces where FDG is not metabolized, such as the blood pool. Model selection was performed for a range of tissue ROIs and voxel TACs by fitting a 0-tissue 1-parameter (where v_b was the only non-zero parameter), a 1-tissue 3-parameter, and an irreversible 2-tissue 4-parameter model (k_4 = 0); the model with the lowest Akaike Information Criterion was chosen. For comparison, parametric Patlak plots (*19*) were generated with and without using the JE delay estimates from

model selection. All results were obtained using a non-linear least-squares fitting process as described previously (*20*). Initialization parameters are included in Supplemental Table 1. To assess the impact of delay correction methods, delay was estimated jointly (JE), via the leading edge (LE) method, or not at all (no delay correction). The first 36 dynamic frames, representing the first 120 seconds of the acquisition, were used to jointly estimate delay prior to fitting all 66 timepoints for estimation of the rest of the parameters. For ROI-based analysis, the same LE thresholds used in simulations (between 2.5 and 50% of the peak activity in the first 2 minutes) were used to determine the IDIF bolus arrival time t_0 and arrival time at the tissue t_d. Both JE and LE estimates of delay (t_d - t_0) were estimated in 1-second steps, and were constrained to be between zero and 50 seconds. The conventional JE method was considered ground truth, such that the optimal LE threshold could be determined across a variety of ROIs. After determining the optimal LE threshold, a single LE threshold was used for kinetic modeling, and the quality of ROI-based and parametric image-derived parameter estimates was assessed using Pearson's *r*.

ROIs were identified in six tissue types: grey matter, liver, lungs, muscle, myocardium, spleen, in addition to the left ventricle blood pool. An additional 28 GUC lesions were delineated based on a threshold of 41% of the maximum standardized uptake value, as recommended by Boellaard *et al*. (*21*). All ROIs were manually corrected for subject motion. ROI delineation was performed using PMOD (PMOD Technologies, Zurich, Switzerland).

In order to highlight a variety of tissue types for prototyping of the method, parametric maps of delay and other kinetic parameters (v_b, K_1, K_i) were generated with both JE and LE methods using the entire image volumes of one representative healthy and one GUC subject. The tissue ROIs listed above were used to generate tissue-specific voxel-wise parameter

estimates from the parametric images (Supplemental Fig. 2). A vascular ROI was also included to assess the impact of delay within the blood pool in the parametric images.

RESULTS

Simulations

Delay estimates were determined for different framing schemes and noise levels (e.g. Supplemental Fig. 1). From the wide range of LE thresholds and CFD attenuation fractions tested, LE results indicate that higher noise levels resulted in only marginal increases in bias and standard deviation, particularly with 2-second frames and a LE threshold of less than 15%, while CFD bias and standard deviation increased with higher noise levels for attenuation fractions of 15% or less (Supplemental Table 2). With 2-second frames, there was less than a 1-second bias in delay for all LE thresholds of 10% or greater, and a 30% LE threshold led to the lowest bias in delay (0.11-0.18 seconds, Supplemental Table 2, bold). As frame length increases from 2 to 10 seconds, the effect of frame length dominates the bias, particularly at higher LE thresholds and higher CFD attenuation fractions. This was mitigated for LE results by increasing the LE threshold to 25% or greater, which reduced bias to < 5 seconds for all noise levels. With a 30% LE threshold, absolute biases for 10 second frames are between 3.80 and 3.96 seconds for all noise levels tested. The CFD method was not investigated further due to its poorer performance on noisy simulated data and reliance on a user-chosen time shift, traditionally based on waveform rise-time (*11*). The LE method does not rely directly on the rise-time, making it the more practical method for total-body PET human subject data. Supplemental Table 3 expands upon the LE results showing data for additional frame lengths. The impact of frame length dominates the bias estimates for large (5- and 10-second) frames and were within 0.5 seconds

of each other across the different noise levels at the same LE threshold.

Although a LE threshold of 25% was the most insensitive to noise level, and a threshold of 30% resulted in the lowest biases and standard deviations for 2-second frames, the simulations focus solely on a grey matter TAC with an ideal bolus injection. Therefore, to assess the performance of the LE method on different tissue types with varying kinetics and the effect of time walk on LE estimates in slowly rising TACs (e.g. liver), a variety of LE thresholds were tested in human ROI-based analyses.

Human ROI-based Analysis

Tissue-specific TACs were consistent across organ type among subjects (Fig. 1, Supplemental Fig. 3). The subset of the 28 lesion TACs shown in Fig. 1 demonstrates the heterogeneity of tracer arrival time and metabolism. Since there were no noticeable differences between healthy subject and GUC patient TACs, ROI-based parameter estimates were pooled across the 14 healthy subjects and 7 GUC patients. Average JE and LE delay estimates with their standard errors (Fig. 2A, 2B) demonstrate the impact of slower TAC rise-times on the LE estimates of liver and muscle, as compared to grey matter, spleen, and GUC lesions, which all demonstrate a sharp rising edge (Supplemental Fig. 3). Based on simulation results and the timing walk, or overestimation of delay that occurs for more slowly-rising TACs as LE thresholds are increased in Fig. 2B, a LE threshold of 10% was selected for further ROI-based results and implemented for parametric imaging. As shown in Fig. 2C, there was good agreement between JE and LE methods in the estimation of delay (Pearson's r=0.96, P<1E-3, slope: 1.00) with a 10% LE threshold for all ROIs.

The impact of delay correction can be seen in Table 1 where parameter estimates were obtained with and without delay correction. With LE-based delay estimation, mean parameter

estimates were in agreement with JE results for v_b (r=0.96, P<1E-3, slope: 0.98), K_i (r=1.00, P<1E-3, slope: 0.99), and K_1 (r=0.97, P<1E-3, slope: 0.91) when all regions were pooled (N=154) (Table 1, top, Supplemental Fig. 4). When delay correction is not performed, there is little impact on K_i (r=1.00, P<1E-3, slope: 1.02), however v_b (r=0.86, P<1E-3, slope: 0.85) and K_1 (r=0.89, P<1E-3, slope: 0.89) are poorly estimated in some tissues, including grey matter, spleen, and GUC lesions. When tissues with negative or zero delay (myocardium, lung) are excluded from pooled analyses, K_i remains constant while there is a drop in v_b (69.4%), and K_1 (4.8%) without delay correction (Table 1).

Table 2 shows the mean and standard deviation estimates of the 42 tissue-parameter pairs. LE estimates were strongly in agreement with JE methods for most tissues, where only five of 38 statistically significant comparisons had a Pearson's r < 0.8, though the LE method did not agree with JE results in some liver and spleen ROIs when estimating v_b.

Parametric Imaging

Voxel-wise LE results were assessed using datasets from one representative healthy volunteer and one representative GUC subject. Using a high-performance computational node (Intel Xeon Gold 2.6 GHz, 24-core processor), JE were produced at an approximate rate of 180 voxels/s, while LE parametric images were produced at an approximate rate of 1,200 voxels/s, representing a 6.7-fold increase in computational efficiency. Parametric results were in agreement with ROI-based methods, though were slightly overestimated for both JE (r=0.97, P<1E-3, slope: 1.05) and LE (r=0.99, P<1E-3, slope: 1.06) (Supplemental Fig. 5). Example delay and K_i maps are shown in Fig. 3. LE-derived delay maps showed some artifacts near the injection site compared to JE delay maps, but results were broadly comparable across most tissues. K_i was similar between JE and LE, and demonstrated improved K_i contrast in the liver

and GUC lesions (arrows) compared to K_i computed with no delay correction or via Patlak plot (Fig. 3, Supplemental Table 4). GUC subject maximum intensity projection images of K_1 and v_b are shown in Fig. 4, where delay correction improved visualization of lesions in the thorax, lower torso, and legs. Like the ROI-based results in Tables 1 and 2, voxel-level delay correction resulted in improved estimation of lesion v_b and K_1 (Fig. 4), which are both sensitive to the early phases of the scan.

Both representative subjects showed some disagreement of LE delay in the muscle and spleen relative to JE delay, though this did not greatly impact K_i or v_b estimates. Scatter plots comparing JE and LE results in a representative healthy subject (Supplemental Fig. 6) demonstrate agreement in the estimation of delay (r=0.99, P<1E-3, slope: 1.01). Estimates of v_b (r=1.00, P<1E-3, slope: 1.00) and K_i (r=1.00, P<1E-3, slope: 0.99) were in strong agreement with JE results. Although not shown, K_1 LE estimates also agreed with JE, but were underestimated (r=0.97, P<1E-3, slope: 0.91).

GUC voxel-wise estimates of delay were similarly in disagreement in some muscle, spleen, and lesion voxels, and overall, delay was slightly overestimated (r=0.99, P<1E-3, slope: 1.10) (Fig. 5). There was strong agreement for v_b (r=1.00, P<1E-3, slope: 0.98) and K_i (r=1.00, P<1E-3, slope: 1.00). Although not shown, GUC subject K_1 estimates were also in agreement (r=0.99, P<1E-3, slope: 0.97).

DISCUSSION

Here we demonstrate, at both the ROI and voxel level, the feasibility of using pulse timing methods (LE and CFD) as a surrogate for jointly estimating tracer delay using the first 120 seconds of data, across a wide range of tissue types present in total-body PET datasets. Noise,

in addition to temporal framing, plays an important role in the choice of threshold in the LE method. In simulations, LE with a 10% threshold or greater provided satisfactory delay bias and standard deviation in short frames at most noise levels, but a 30% threshold resulted in the lowest measured bias and standard deviation at all noise levels. However, the shape of the TAC itself is important, and may explain the discrepancies between simulations and acquired TACs in determining the optimal LE threshold for grey matter. Further, tissues with a long rise-time such as the liver suffer from time walk, and spillover from the blood pool can cause early triggering. Threshold optimization may be necessary for these tissues. Since the simulation data showed no advantage in using the CFD approach, the simpler LE method was used for human studies.

After assessing regional delay estimates from various LE thresholds, a 10% threshold was implemented for all human analyses. JE and LE methods were in agreement for all estimated kinetic parameters at both ROI and voxel levels. v_b and K_1 estimates were sensitive to delay correction, while K_i was only impacted by delay correction in the liver and GUC lesions of the parametric images. Improved estimation of v_b and K_1 has implications for perfusion imaging with radiotracers with rapid kinetics (e.g. ^{15}O-water).

The bolus shape is another important consideration; the simulation results indicate that LE methods work well with a sharp bolus peak for the IF with respect to the frame length, such that there is as little timing walk in the tissue and IF curves as possible. Therefore these methods are expected to be translatable to other tracers delivered via bolus injection.

Although we implemented model selection in our parametric analyses, special-case tissues (e.g. liver, lung) require additional models that consider dual input functions and dispersion which were not implemented here, but will be a part of our future work. Patient motion is another major challenge with total-body parametric imaging. Short frames capture

respiratory and cardiac motion, while any gross motion throughout the scan is also captured. In practice, application of these methods will likely benefit greatly from incorporation of motion correction in total-body PET (*22*). Here, we performed simple manual correction of our ROIs, and selected image datasets with limited motion for parametric analysis.

While LE delay correction can be implemented with the Patlak analysis, delay correction has a limited impact on Patlak K_i, indicating that improved lesion contrast seen in this study was a result of implementation of compartment modeling with delay correction.

CONCLUSION

In this work we apply pulse timing methods to dynamic PET images to estimate the arrival time of the radiotracer bolus in ROIs and in every voxel in the body. We have demonstrated that pulse timing methods can be an efficient surrogate for JE. Moreover, LE and JE methods of delay correction provided K_i, v_b, and K_1 estimates that were in good agreement and substantially improved parametric results compared to when no delay correction was performed, or compared to Patlak analysis. Further, at the voxel level, LE estimates were in agreement with JE across a variety of tissue types for both healthy and GUC subjects. The results suggest delay correction should be implemented for total-body PET kinetic modeling using short (<5 second) frames, and implementing the LE method instead of JE will allow for efficient correction of delay.

DISCLOSURE

This work was supported by NIH R01 CA206187 and R35 CA197608. UC Davis has a research agreement and a sales-based revenue sharing agreement with United Imaging Healthcare. No other potential conflicts of interest relevant to this article exist.

ACKNOWLEDGEMENTS

The authors thank the EXPLORER team members and technologists for their contributions to this work.

KEY POINTS

QUESTION: Are pulse timing methods an efficient surrogate for joint estimation (JE) of the delay in tracer arrival time for total-body PET kinetic modeling?

PERTINENT FINDINGS: Results from regional and voxel-wise studies in 21 subjects (14 healthy volunteers, 7 cancer patients) showed strong agreement between leading edge (LE) and JE methods in estimating delay and kinetic parameters v_b, K_i, and K_1. Improved regional estimates, as well as increased parametric image contrast of v_b and K_1 were observed when delay correction was performed.

IMPLICATIONS FOR PATIENT CARE: This study demonstrates the importance of delay correction in total-body PET kinetic modeling, and that LE delay correction can be a computationally efficient surrogate for JE, making the methods more translatable for patient studies.

REFERENCES

1. Lammertsma AA. Essentials of Quantitative Imaging with PET. In: Volterrani D, Erba PA, Carrió, I, Strauss HW, Mariani G, eds. *Nuclear Medicine Textbook*. Cham, Switzerland: Springer; 2019:219-233.
2. Iida H, Kanno I, Miura S, Murakami M, Takahashi K, Uemura K. Error analysis of a quantitative cerebral blood flow measurement using H215O autoradiography and positron emission tomography, with respect to the dispersion of the input function. *J Cereb Blood Flow Metab*. 1986;6:536-545.
3. Islam MM, Tsujikawa T, Mori T, Kiyono Y, Okazawa H. Pixel-by-pixel precise delay correction for measurement of cerebral hemodynamic parameters in H215O PET study. *Ann Nucl Med*. 2017;31:283-294.
4. Feng T, Zhao Y, Shi H, et al. Total-body quantitative parametric imaging of early kinetics of 18F-FDG. *J Nucl Med*. 2021;62:738-744.
5. Cherry SR, Badawi RD, Karp JS, Moses WW, Price P, Jones T. Total-body imaging: Transforming the role of positron emission tomography. *Sci Transl Med*. 2017;9:eaaf6169.
6. Zhang X, Cherry SR, Xie Z, Shi H, Badawi RD, Qi J. Subsecond total-body imaging using ultrasensitive positron emission tomography. *Proc Natl Acad Sci*. 2020;117:2265-2267.
7. Iida H, Law I, Pakkenberg B, et al. Quantitation of regional cerebral blood flow corrected for partial volume effect using O-15 water and PET: I. Theory, error analysis, and stereologic comparison. *J Cereb Blood Flow Metab*. 2000;20:1237-1251.
8. Iida H, Kanno I, Takahashi A, et al. Measurement of absolute myocardial blood flow with H215O and dynamic positron-emission tomography. Strategy for quantification in relation to the partial-volume effect. *Circulation*. 1988;78:104-115.
9. Meyer E. Simultaneous correction for tracer arrival delay and dispersion in CBF measurements by the H215O autoradiographic method and dynamic PET. *J Nucl Med*. 1989;30:1069-1078.
10. Lammertsma AA, Cunningham VJ, Deiber MP, et al. Combination of dynamic and integral methods for generating reproducible functional CBF images. *J Cereb Blood Flow Metab*. 1990;10:675-686.
11. Knoll GF. *Radiation Detection and Measurement*. New York, NY: John Wiley & Sons, Inc. 2005;659-662.

12. Feng D, Huang SC, Wang X. Models for computer simulation studies of input functions for tracer kinetic modeling with positron emission tomography. *Int J Biomed Comput*. 1993;32:95-110.

13. Feng D, Wong KP, Wu Chi-Ming, Siu WC. A technique for extracting physiological parameters and the required input function simultaneously from PET image measurements: Theory and simulation study. *IEEE Trans Inf Technol Biomed*. 1997;1:243-254.

14. Huisman MC, van Golen LW, Hoetjes NJ, et al. Cerebral blood flow and glucose metabolism in healthy volunteers measured using a high-resolution PET scanner. *EJNMMI Res*. 2012;2:1-9.

15. Wu Y, Carson RE. Noise reduction in the simplified reference tissue model for neuroreceptor functional imaging. *J Cereb Blood Flow Metab*. 2002;22:1440-1452.

16. Spencer BA, Berg E, Schmall JP, et al. Performance evaluation of the uEXPLORER total-body PET/CT scanner based on NEMA NU 2-2018 with additional tests to characterize PET scanners with a long axial field of view. *J Nucl Med*. 2021;62:861-870.

17. Leung EK, Berg E, Omidvari N, et al. Quantitative accuracy in total-body imaging using the uEXPLORER PET/CT scanner. *Phys Med Biol*. September 20, 2021 [Epub ahead of print].

18. Wang G, Qi J. PET image reconstruction using kernel method. *IEEE Trans Med Imaging*. 2015;34:61-71.

19. Patlak CS, Blasberg RG, Fenstermacher JD. Graphical evaluation of blood-to-brain transfer constants from multiple-time uptake data. *J Cereb Blood Flow Metab*. 1983;3:1-7.

20. Wang G, Qi J. Generalized algorithms for direct reconstruction of parametric images from dynamic PET data. *IEEE Trans Med Imaging*. 2009;28:1717-1726.

21. Boellaard R, Delgado-Bolton R, Oyen WJG, et al. FDG PET/CT: EANM procedure guidelines for tumour imaging: version 2.0. *Eur J Nucl Med Mol Imaging*. 2015;42:328-354.

22. Wang Y, Li E, Cherry SR, Wang G. Total-body PET kinetic modeling and potential opportunities using deep learning. *PET Clin*. 2021;16:613-625.

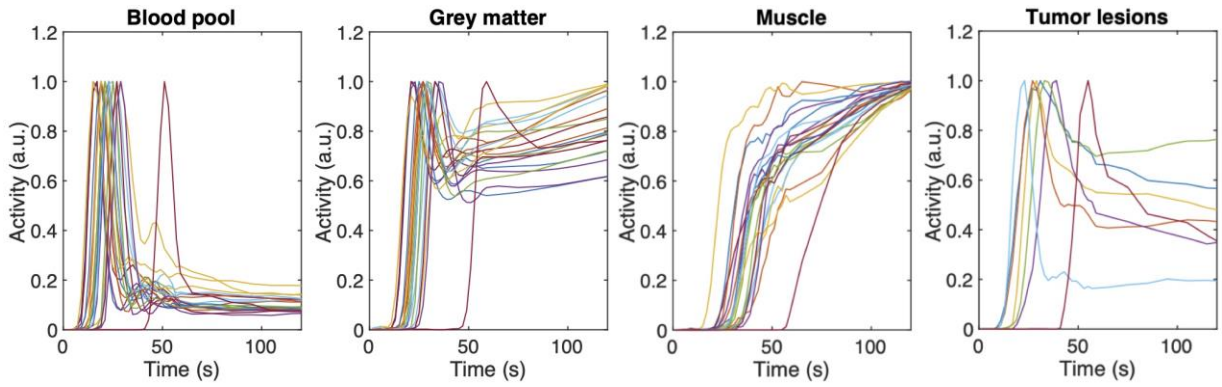

FIGURE 1: Normalized TACs in a number of healthy subject and GUC patient tissues. Although injection bolus shape was consistent across pooled human subjects, injection time relative to the start of the scan, delay in arrival time to individual tissues, and initial lesion uptake differed. A single lesion is shown per GUC patient for ease of visualization.

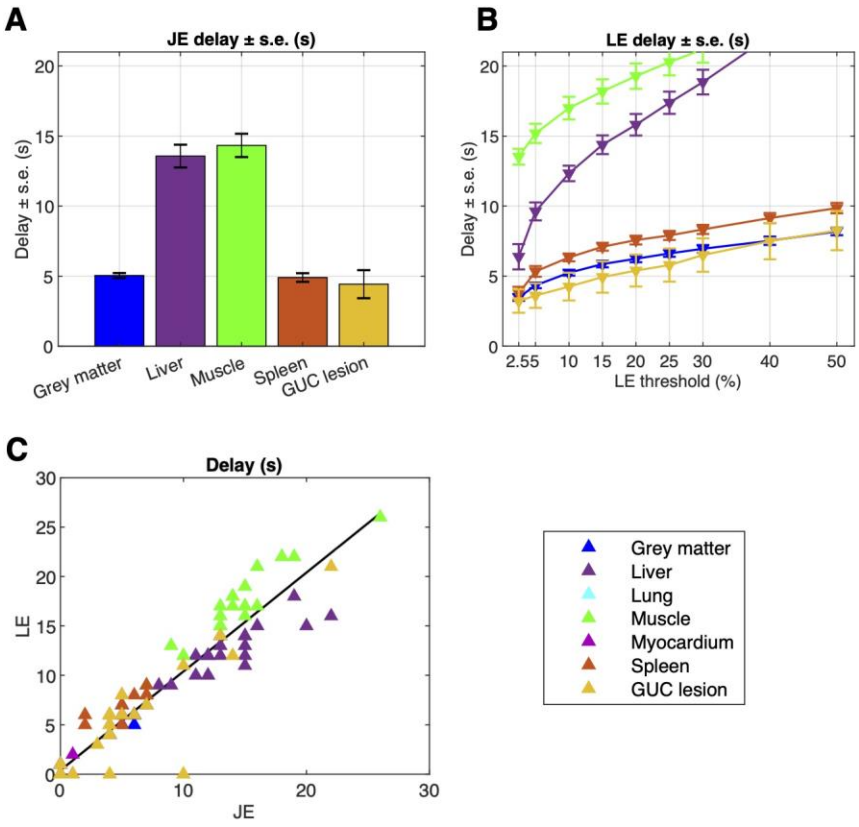

FIGURE 2: Average JE delay estimates with standard error (s.e.) (A), and LE estimates (B) at thresholds ranging from 2.5 to 50% for different ROIs. As LE threshold increases, LE delay estimates exhibit time walk for tissues with longer rise-times such as the liver (▲) and muscle (▲). Based on A and B, a threshold of 10% was selected for further kinetic analyses. The LE method was in good agreement with JE estimates of delay (C, r=0.96, P<1E-3, slope: 1.00) with a 10% threshold across all regions.

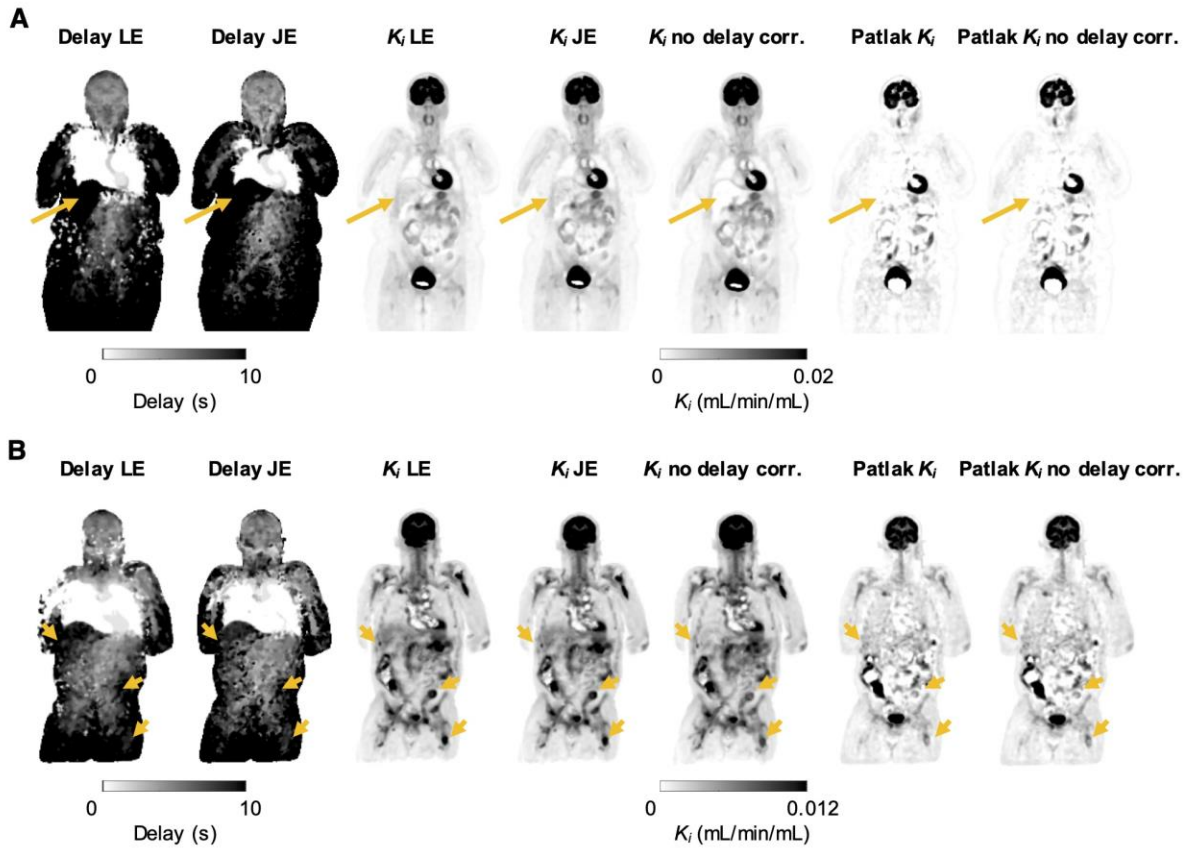

FIGURE 3: Maximum intensity projection (MIP) parametric images of delay and K_i for a representative healthy subject (A) and a GUC patient (B) generated using four coronal slices (1.6 cm thick). 10% LE threshold-derived delay maps showed some differences compared to JE delay maps, particularly close to the injection site, but are broadly in agreement across the rest of the body. Compartment modeling-based K_i maps were similar with JE and LE methods of delay correction, and both methods resulted in improved liver signal (A, arrows) and lesion contrast (B, arrows) compared to Patlak results, or to when no delay correction was implemented.

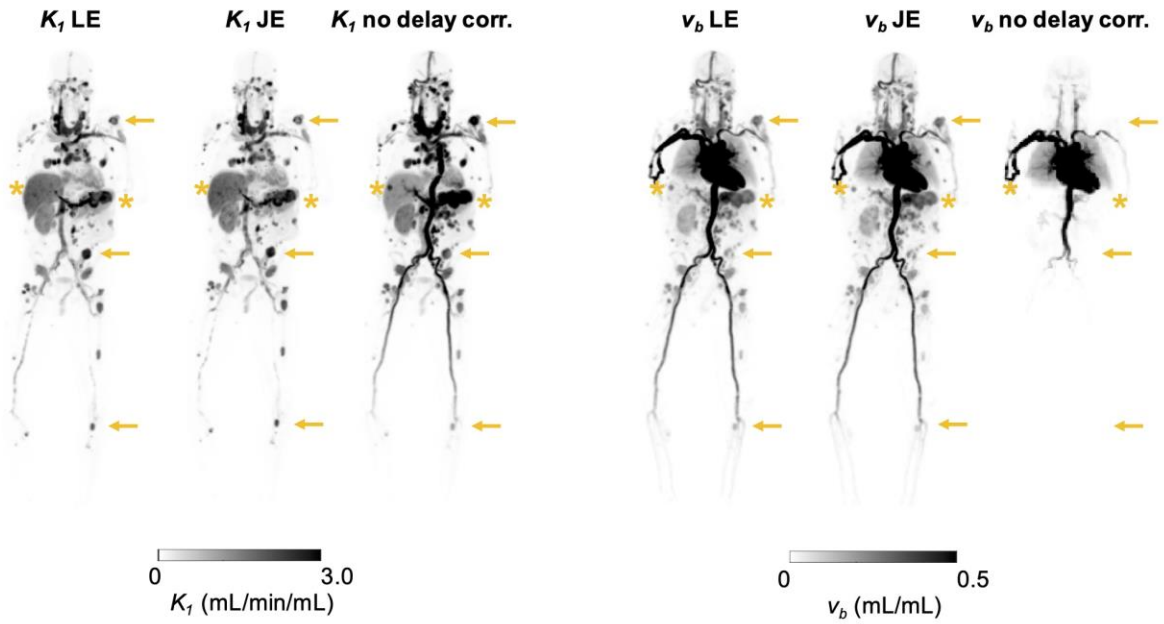

FIGURE 4: MIPs of K_1 (left) and v_b (right) parametric maps for a representative GUC patient. Overall, LE-derived parametric images were similar to JE-based images. Without delay correction, K_1 was increased while v_b was underestimated in much of the abdomen and lower body compared to JE-based v_b. Multiple GUC lesions (arrows) demonstrated increased K_1 and v_b when delay correction was applied, while vessels in the legs and some lesions in the upper abdomen and liver (asterisks) showed a reduction in K_1 and an increase in v_b.

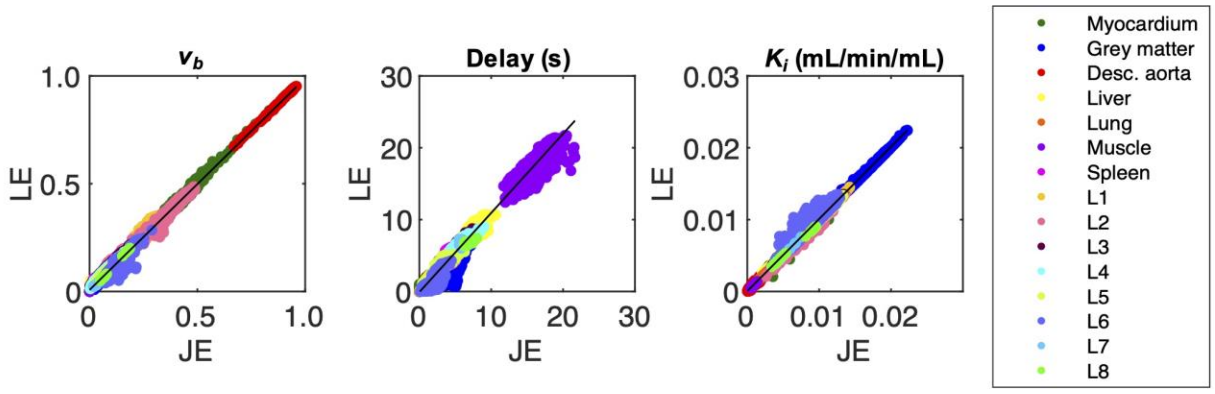

FIGURE 5: Parametric LE versus JE results for a GUC patient were compared across a number of regions including 8 lesions (L1-L8). Delay is slightly overestimated (r=0.99, P<1E-3, slope: 1.10) overall, and is underestimated in a number of TACs, namely from muscle, lesions and grey matter. LE v_b (r=1.00, P<1E-3, slope: 0.98) and K_i (r=1.00, P<1E-3, slope: 1.00) estimates demonstrate nearly 1:1 ratios with JE.

TABLES

TABLE 1: Mean (s.d.) estimated kinetic parameters obtained from pooled regions

	All regions (N=154)					Regions* with positive delay (N=112)				
Parameter	JE		LE		$r^{\dagger}$	JE		LE		$r^{\dagger}$
v_b	0.070	(0.079)	0.076	(0.080)	0.96	0.036	(0.056)	0.044	(0.061)	0.91
K_1	0.553	(0.629)	0.529	(0.584)	0.97	0.600	(0.677)	0.569	(0.618)	0.98
K_i	0.012	(0.017)	0.012	(0.017)	1.00	0.011	(0.014)	0.011	(0.014)	1.00
Delay	5.981	(6.073)	6.377	(6.331)	0.96	8.205	(5.701)	8.732	(5.888)	0.94
k_2	1.213	(1.292)	1.171	(1.277)	0.94	1.133	(1.230)	1.084	(1.188)	0.95
k_3	0.039	(0.069)	0.037	(0.057)	0.97	0.035	(0.064)	0.032	(0.046)	0.96

	All regions (N=154)					Regions* with positive delay (N=112)				
Parameter	JE		No delay corr.		$r^{\dagger}$	JE		No delay corr.		$r^{\dagger}$
v_b	0.070	(0.079)	0.050	(0.078)	0.86	0.036	(0.056)	0.011	(0.036)	0.57
K_1	0.553	(0.629)	0.541	(0.622)	0.89	0.600	(0.677)	0.571	(0.656)	0.88
K_i	0.012	(0.017)	0.012	(0.017)	1.00	0.011	(0.014)	0.011	(0.015)	0.99
Delay	5.981	(6.073)	0	0	N.A.	8.205	(5.701)	0	0	N.A.
k_2	1.213	(1.292)	1.205	(1.348)	0.85	1.133	(1.230)	1.085	(1.233)	0.79
k_3	0.039	(0.069)	0.040	(0.063)	0.96	0.035	(0.064)	0.036	(0.057)	0.94

N.A.: Not available.

*excludes lung and myocardium, †P<1E-3.

TABLE 2: Mean (s.d.) estimated kinetic parameters for healthy subjects (N=14) and GUC patients (N=7)

	Grey Matter					Liver					Lung				
Parameter	JE		LE		*r**	JE		LE		*r**	JE		LE		*r**
v_b	0.030	(0.006)	0.030	(0.006)	0.98	0.001	(0.003)	0.001	(0.005)	N.S.	0.128	(0.039)	0.128	(0.039)	1.00
K_1	0.107	(0.017)	0.107	(0.018)	1.00	0.660	(0.286)	0.636	(0.291)	0.98	0.023	(0.012)	0.023	(0.012)	1.00
K_i	0.031	(0.007)	0.031	(0.007)	1.00	0.002	(0.002)	0.002	(0.001)	0.81	0.000	(0.000)	0.000	(0.000)	1.00
Delay	5.048	(0.805)	5.238	(0.944)	0.77	13.571	(3.723)	12.333	(2.536)	0.87	0.000	(0.000)	0.000	(0.000)	N.A.
k_2	0.165	(0.027)	0.163	(0.029)	0.95	0.765	(0.374)	0.737	(0.381)	0.98	0.205	(0.090)	0.205	(0.090)	1.00
k_3	0.067	(0.012)	0.066	(0.013)	0.99	0.002	(0.002)	0.002	(0.002)	0.84	0.001	(0.004)	0.001	(0.004)	1.00
	Muscle					**Myocardium**					**Spleen**				
Parameter	JE		LE		*r**	JE		LE		*r**	JE		LE		*r**
v_b	2.3E-4	(4.7E-4)	0.001	(0.001)	0.69	0.190	(0.063)	0.192	(0.068)	0.98	0.044	(0.025)	0.083	(0.029)	N.S.
K_1	0.026	(0.012)	0.026	(0.012)	1.00	0.832	(0.307)	0.820	(0.356)	0.81	1.593	(0.556)	1.458	(0.467)	0.99
K_i	0.002	(0.000)	0.002	(0.000)	1.00	0.029	(0.024)	0.028	(0.024)	1.00	0.003	(0.001)	0.003	(0.001)	0.99
Delay	14.333	(3.812)	17.000	(3.715)	0.94	0.095	(0.301)	0.190	(0.512)	N.S.	4.905	(1.411)	6.333	(1.278)	0.71
k_2	0.249	(0.142)	0.249	(0.136)	1.00	2.651	(1.044)	2.597	(1.215)	0.78	2.867	(0.980)	2.709	(0.882)	1.00
k_3	0.016	(0.006)	0.016	(0.006)	1.00	0.099	(0.088)	0.098	(0.088)	1.00	0.006	(0.003)	0.006	(0.003)	0.99
	GUC lesions (N=28)														
Parameter	JE		LE		*r**										
v_b	0.089	(0.086)	0.089	(0.092)	0.93										
K_1	0.609	(0.614)	0.605	(0.573)	0.92										
K_i	0.017	(0.016)	0.018	(0.016)	0.99										
Delay	4.429	(5.295)	4.250	(5.254)	0.90										
k_2	1.496	(1.213)	1.443	(1.272)	0.79										
k_3	0.071	(0.114)	0.062	(0.074)	0.97										

N.A.: Not available. N.S.: Not significant.

* P<1E-3.

GRAPHICAL ABSTRACT

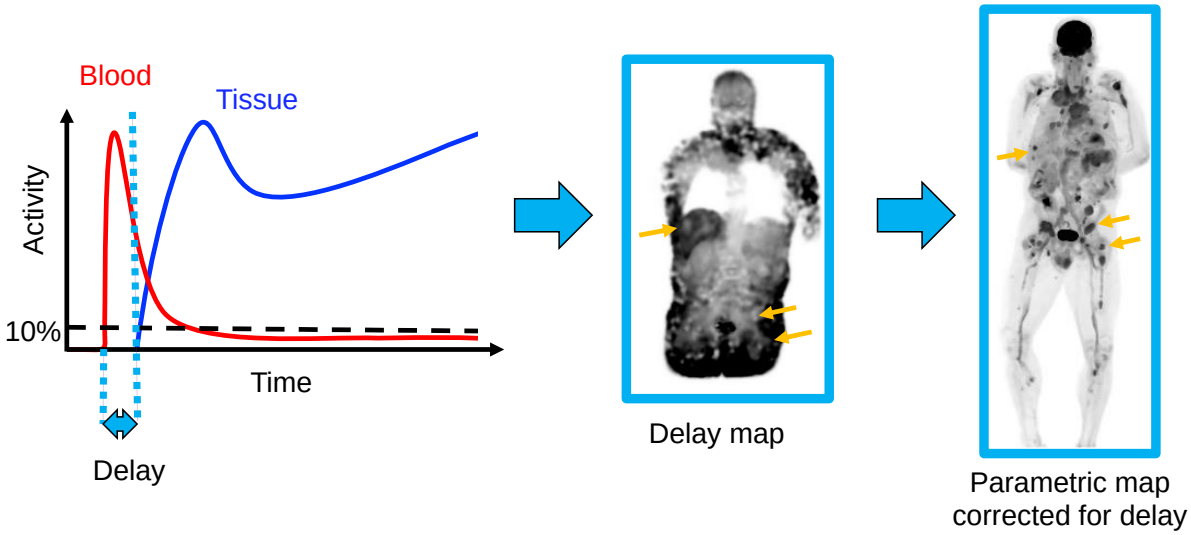

SUPPLEMENTAL TABLE 1: Initialization parameters for non-linear least squares fitting

Parameter	v_b *(mL/mL)*	K_1 *(mL/min/mL)*	k_2 *(min^{-1})*	k_3 *(min^{-1})*	k_4 *(min^{-1})*	*Delay (s)*
Initial value	0.01	0.01	0.01	0.01	-	0
Upper bound	1.0	5.0	5.0	1.0	-	50
Lower bound	0.0001	0.0	0.0	0.0	-	0

SUPPLEMENTAL TABLE 2: Absolute bias (s.d.) in seconds of LE and CFD delay estimates for 2- and 10-second frame lengths

	LE								***CFD***							
Noise Level	0.03		0.1		0.2		0.3		0.03		0.1		0.2		0.3	
Threshold/ Attenuation fraction	**LE, 2 s frames**								**CFD, 2 s frames**							
2.5%	1.49	(0.38)	1.54	(0.39)	1.61	(0.63)	5.93	(9.99)	5.24	(13.14)	13.71	(19.38)	22.28	(20.22)	27.97	(18.52)
5%	1.23	(0.33)	1.25	(0.34)	1.29	(0.35)	1.33	(0.37)	0.74	(2.85)	5.63	(13.71)	11.75	(18.46)	16.62	(19.99)
10%	0.88	(0.24)	0.89	(0.25)	0.91	(0.27)	0.93	(0.29)	0.62	(0.41)	0.64	(0.98)	2.43	(8.30)	5.53	(13.29)
15%	0.61	(0.21)	0.62	(0.22)	0.63	(0.23)	0.64	(0.26)	0.67	(0.46)	0.69	(0.47)	0.71	(0.82)	1.19	(4.31)
20%	0.39	(0.17)	0.40	(0.18)	0.40	(0.20)	0.41	(0.22)	0.80	(0.53)	0.79	(0.52)	0.79	(0.52)	0.79	(0.72)
25%	0.20	(0.13)	0.21	(0.14)	0.22	(0.15)	0.24	(0.17)	0.87	(0.55)	0.87	(0.55)	0.87	(0.55)	0.86	(0.55)
30%	**0.11**	**(0.05)**	**0.11**	**(0.07)**	**0.14**	**(0.10)**	**0.18**	**(0.13)**	0.94	(0.56)	0.93	(0.56)	0.93	(0.56)	0.93	(0.57)
40%	0.32	(0.09)	0.32	(0.12)	0.34	(0.17)	0.35	(0.21)	1.00	(0.56)	1.04	(0.57)	1.06	(0.58)	1.07	(0.59)
50%	0.63	(0.09)	0.63	(0.12)	0.65	(0.19)	0.67	(0.25)	1.18	(0.58)	1.18	(0.58)	1.20	(0.60)	1.20	(0.61)
Threshold/ Attenuation fraction	**LE, 10 s frames**								**CFD, 10 s frames**							
2.5%	8.46	(2.34)	8.64	(2.39)	8.95	(2.65)	15.13	(11.40)	4.27	(7.53)	7.36	(11.87)	14.44	(16.73)	20.69	(17.57)
5%	7.70	(2.22)	7.81	(2.25)	7.99	(2.28)	8.20	(2.32)	2.73	(1.59)	5.16	(9.26)	6.65	(11.03)	10.10	(14.31)
10%	6.65	(2.04)	6.74	(2.06)	6.86	(2.08)	6.99	(2.10)	2.78	(1.66)	2.78	(1.67)	4.08	(6.63)	5.02	(8.36)
15%	5.84	(1.94)	5.91	(1.96)	6.00	(1.99)	6.09	(2.00)	2.94	(1.86)	2.95	(1.86)	2.94	(1.86)	3.06	(2.59)
20%	5.14	(1.82)	5.20	(1.84)	5.28	(1.86)	5.35	(1.88)	3.01	(1.94)	3.01	(1.94)	3.01	(1.93)	3.01	(1.93)
25%	4.47	(1.71)	4.52	(1.73)	4.59	(1.75)	4.65	(1.77)	3.05	(1.98)	3.06	(1.98)	3.06	(1.98)	3.06	(1.98)
30%	3.80	(1.64)	3.85	(1.65)	3.91	(1.67)	3.96	(1.69)	3.10	(2.02)	3.10	(2.02)	3.09	(2.01)	3.09	(2.01)
40%	2.50	(1.59)	2.54	(1.60)	2.59	(1.62)	2.63	(1.63)	3.10	(2.02)	3.10	(2.02)	3.10	(2.02)	3.12	(2.04)
50%	1.58	(1.30)	1.61	(1.31)	1.64	(1.33)	1.66	(1.34)	3.21	(2.12)	3.18	(2.10)	3.21	(2.12)	3.25	(2.15)

SUPPLEMENTAL TABLE 3: Absolute bias (s.d.) of delay estimates (s) across different LE thresholds, framing protocols, noise levels

Noise Level (Sc)	0.03		0.1		0.2		0.3	
Framing (s)				**5% LE**				
0.1 (Native)	0.03	(0.01)	0.03	(0.02)	1.83	(6.89)	11.06	(15.0)
1	0.54	(0.14)	0.55	(0.15)	0.56	(0.17)	0.58	(0.27)
2	1.23	(0.33)	1.25	(0.34)	1.29	(0.35)	1.33	(0.37)
5	3.58	(0.85)	3.64	(0.86)	3.73	(0.90)	3.82	(0.94)
10	7.70	(2.22)	7.81	(2.25)	7.99	(2.28)	8.20	(2.32)
				10% LE				
0.1 (Native)	0.01	(0.01)	0.03	(0.03)	0.06	(0.06)	0.08	(0.09)
1	0.32	(0.10)	0.32	(0.11)	0.32	(0.13)	0.32	(0.16)
2	0.88	(0.24)	0.89	(0.25)	0.91	(0.27)	0.93	(0.29)
5	2.88	(0.72)	2.92	(0.74)	2.97	(0.76)	3.04	(0.78)
10	6.65	(2.04)	6.74	(2.06)	6.86	(2.08)	6.99	(2.10)
				20% LE				
0.1 (Native)	0.08	(0.02)	0.13	(0.07)	0.18	(0.12)	0.21	(0.15)
1	0.06	(0.04)	0.06	(0.05)	0.09	(0.07)	0.12	(0.09)
2	0.39	(0.17)	0.40	(0.18)	0.40	(0.20)	0.41	(0.22)
5	1.89	(0.65)	1.92	(0.66)	1.95	(0.67)	2.00	(0.69)
10	5.14	(1.82)	5.20	(1.84)	5.28	(1.86)	5.35	(1.88)
				25% LE				
0.1 (Native)	0.14	(0.03)	0.21	(0.09)	0.26	(0.15)	0.30	(0.19)
1	0.09	(0.05)	0.10	(0.06)	0.14	(0.09)	0.16	(0.13)
2	0.20	(0.13)	0.21	(0.14)	0.22	(0.15)	0.24	(0.17)
5	1.51	(0.64)	1.53	(0.64)	1.56	(0.65)	1.60	(0.67)
10	4.47	(1.71)	4.52	(1.73)	4.59	(1.75)	4.65	(1.77)
				30% LE				
0.1 (Native)	0.22	(0.04)	0.30	(0.11)	0.36	(0.18)	0.40	(0.22)
1	0.19	(0.05)	0.21	(0.07)	0.24	(0.12)	0.26	(0.16)
2	0.11	(0.05)	0.11	(0.07)	0.14	(0.10)	0.18	(0.13)
5	1.16	(0.61)	1.18	(0.61)	1.21	(0.63)	1.23	(0.64)
10	3.80	(1.64)	3.85	(1.65)	3.91	(1.67)	3.96	(1.69)
				40% LE				
0.1 (Native)	0.40	(0.05)	0.50	(0.14)	0.58	(0.24)	0.64	(0.30)
1	0.40	(0.04)	0.42	(0.07)	0.46	(0.14)	0.50	(0.21)
2	0.32	(0.09)	0.32	(0.12)	0.34	(0.17)	0.35	(0.21)
5	0.64	(0.40)	0.65	(0.42)	0.66	(0.45)	0.67	(0.48)
10	2.50	(1.59)	2.54	(1.60)	2.59	(1.62)	2.63	(1.63)
				50% LE				
0.1 (Native)	0.61	(0.06)	0.74	(0.18)	0.85	(0.31)	0.93	(0.40)
1	0.61	(0.05)	0.63	(0.09)	0.69	(0.17)	0.75	(0.27)
2	0.63	(0.09)	0.64	(0.12)	0.65	(0.19)	0.67	(0.25)
5	0.50	(0.30)	0.51	(0.30)	0.52	(0.30)	0.54	(0.32)
10	1.58	(1.30)	1.61	(1.32)	1.64	(1.33)	1.67	(1.35)

SUPPLEMENTAL TABLE 4: Impact of delay correction on mean parametric Patlak K_i (mL/min/100 mL) for representative GUC patient

Tissue	*JE*	*LE*	*No delay correction*
Grey matter	1.253	1.250	1.249
Liver	0.118	0.116	0.113
Lung	0.094	0.094	0.094
Muscle	0.051	0.050	0.049
Myocardium	0.252	0.252	0.252
Spleen	0.302	0.302	0.301
L1	0.300	0.300	0.299
L2	0.187	0.187	0.186
L3	0.309	0.308	0.306
L4	0.214	0.213	0.211
L5	0.270	0.269	0.268
L6	0.317	0.316	0.316
L7	0.130	0.129	0.128
L8	0.277	0.277	0.276

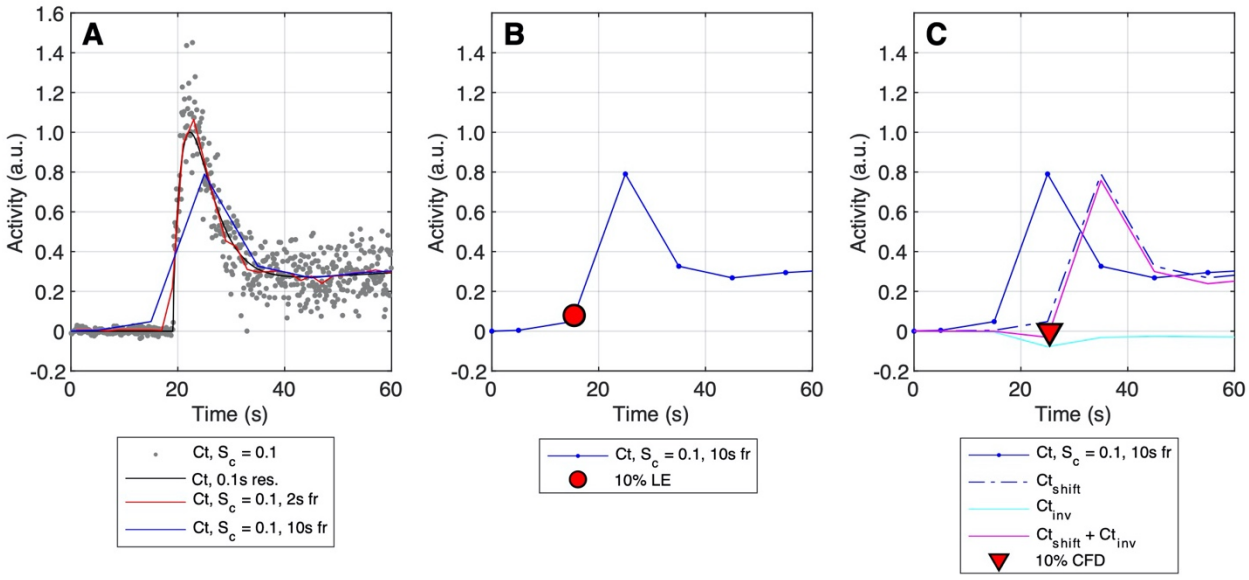

SUPPLEMENTAL FIGURE 1: Time activity curves (TACs) for simulations (A), example LE (B) and CFD (C) delay estimates. In the left panel, a delay of 19.2 seconds was used to shift the IF and generate the ground truth TAC (—). In this example noisy realization (•), the scaling factor of the standard deviation S_c is equal to 0.1. The TACs were then re-binned to reflect different frame lengths. Shown here are 2 (—) and 10 (—) second frames, with example LE (B, ●) and CFD (C, ▼) delay estimates for the 10-second frames. For the LE delay estimation in (B), a 10% LE trigger threshold was selected to mark the time at which the signal amplitude passes the trigger value, which is recorded as the arrival time. For the CFD method in (C), the following three steps were performed: (i) TACs were shifted in time by 2 seconds for shorter framing, or 1 frame when the frame length was greater than 2 seconds (C, Ct_{shift}). (ii) Attenuated and inverted versions of the TAC (attenuated to between 2.5 and 50% of the peak activity) (C, Ct_{inv}) were added to the shifted TAC. (iii) The zero-crossing point, or the timepoint at which the TAC sign changes from negative to positive marks the arrival time (C, ▼).

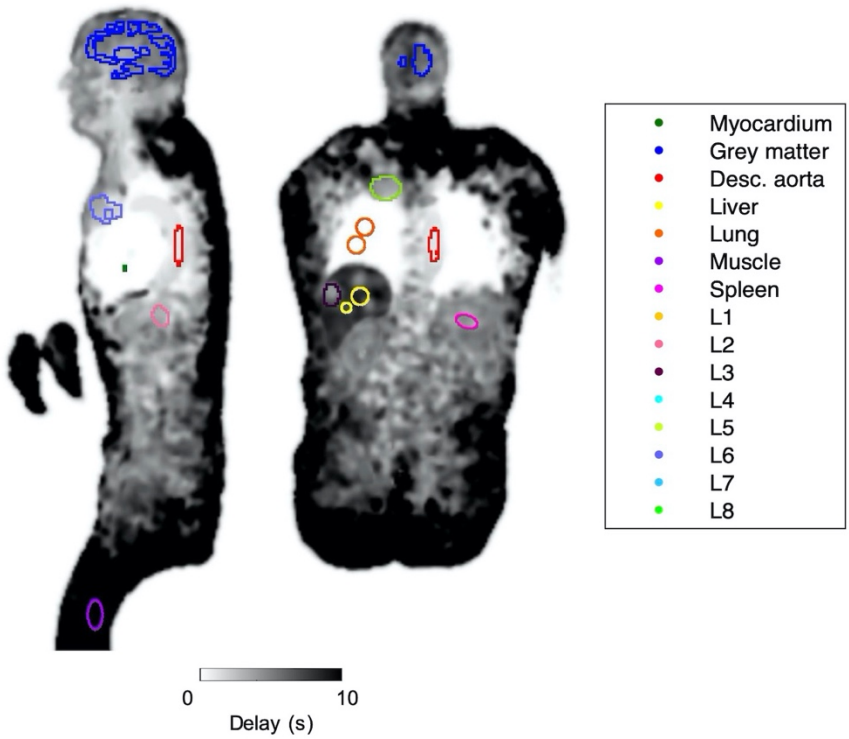

SUPPLEMENTAL FIGURE 2: Cross sectional delay maps with overlay of regions of interest (ROIs) from a number of GUC patient tissues selected for parametric kinetic analysis. As noted in the text, an additional vascular ROI was delineated in order to assess the impact of delay correction within the blood pool. The descending aorta, as shown above, reflects a positive delay value with respect to the left ventricle.

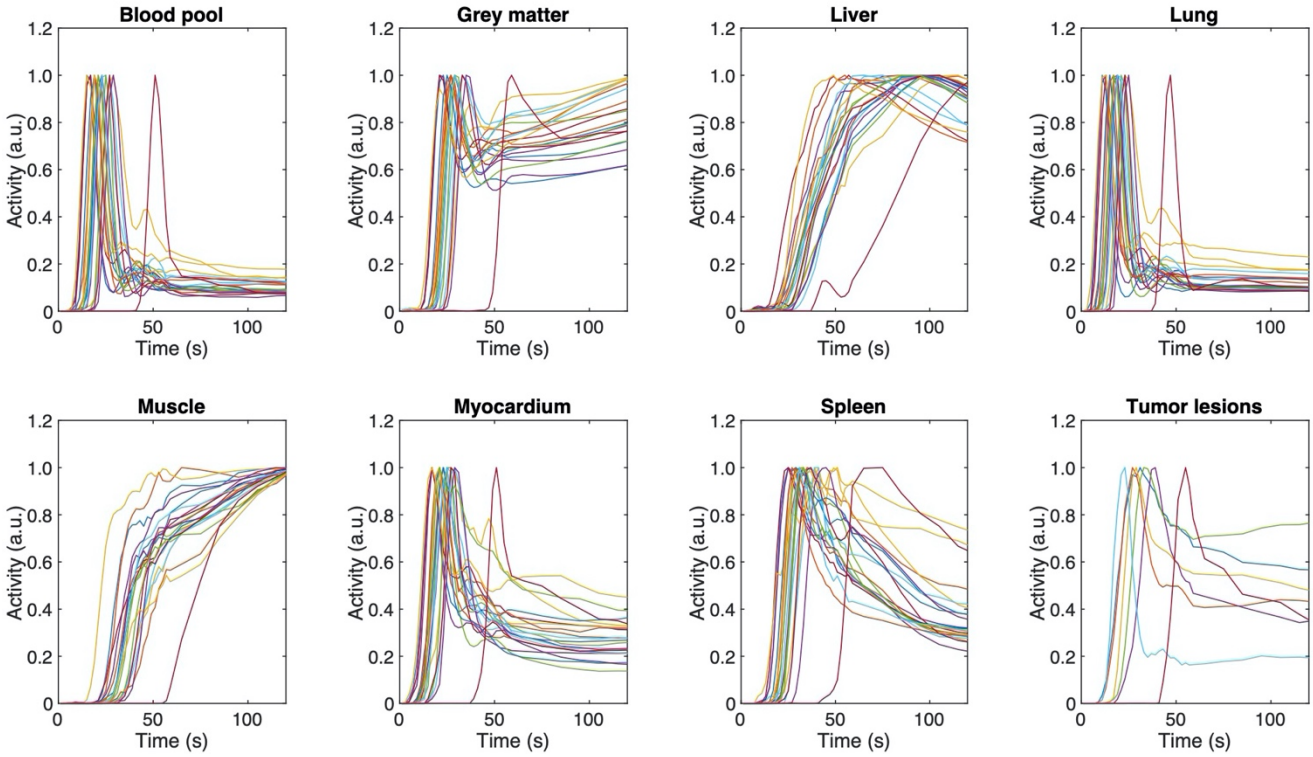
Blood pool
Grey matter
Liver
Lung
Muscle
Myocardium
Spleen
Tumor lesions
Activity (a.u.)
Time (s)
0
0.2
0.4
0.6
0.8
1.0
1.2
0
50
100

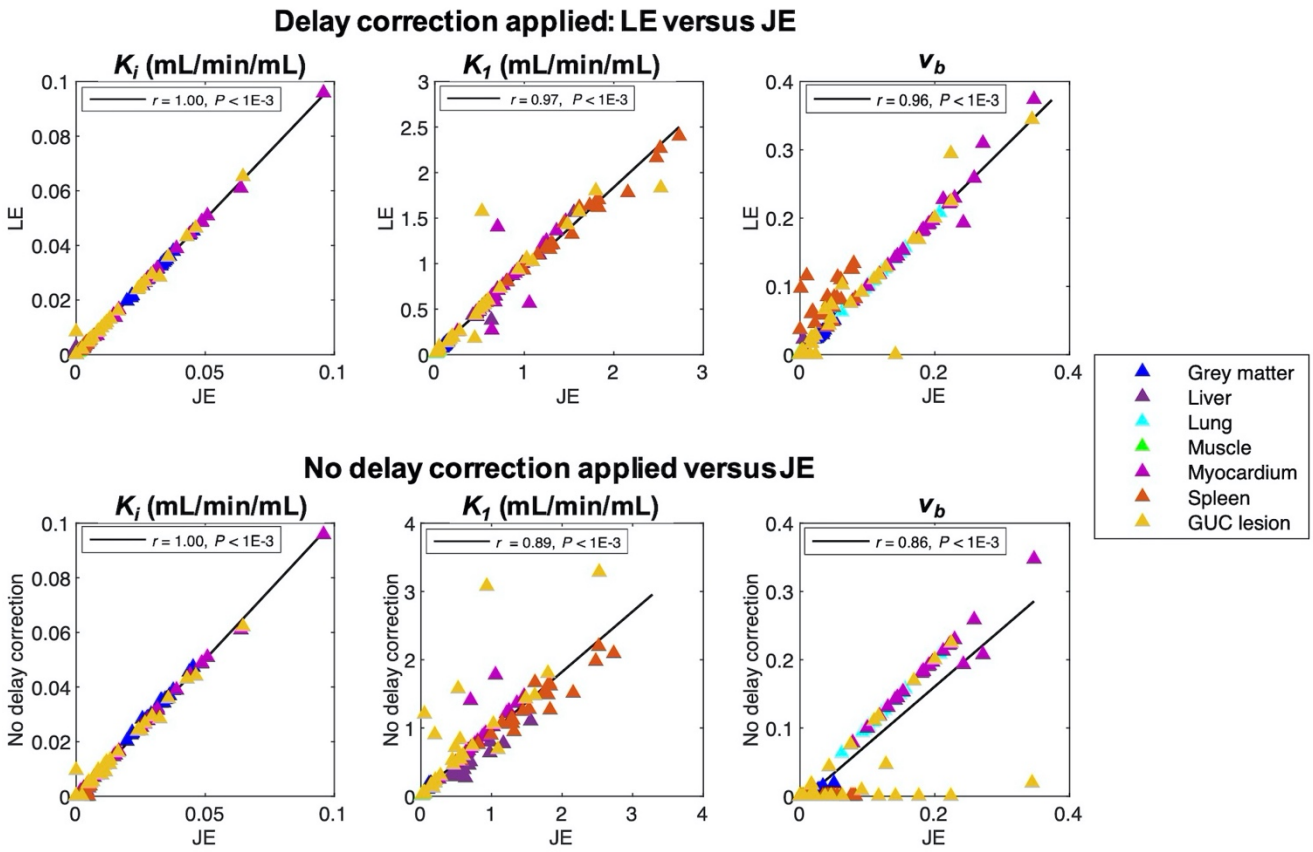
Delay correction applied: LE versus JE
K_i (mL/min/mL)
K_1 (mL/min/mL)
v_b
r = 1.00, P < 1E-3
r = 0.97, P < 1E-3
r = 0.96, P < 1E-3
LE
JE
No delay correction applied versus JE
r = 1.00, P < 1E-3
r = 0.89, P < 1E-3
r = 0.86, P < 1E-3
No delay correction
Grey matter
Liver
Lung
Muscle
Myocardium
Spleen
GUC lesion

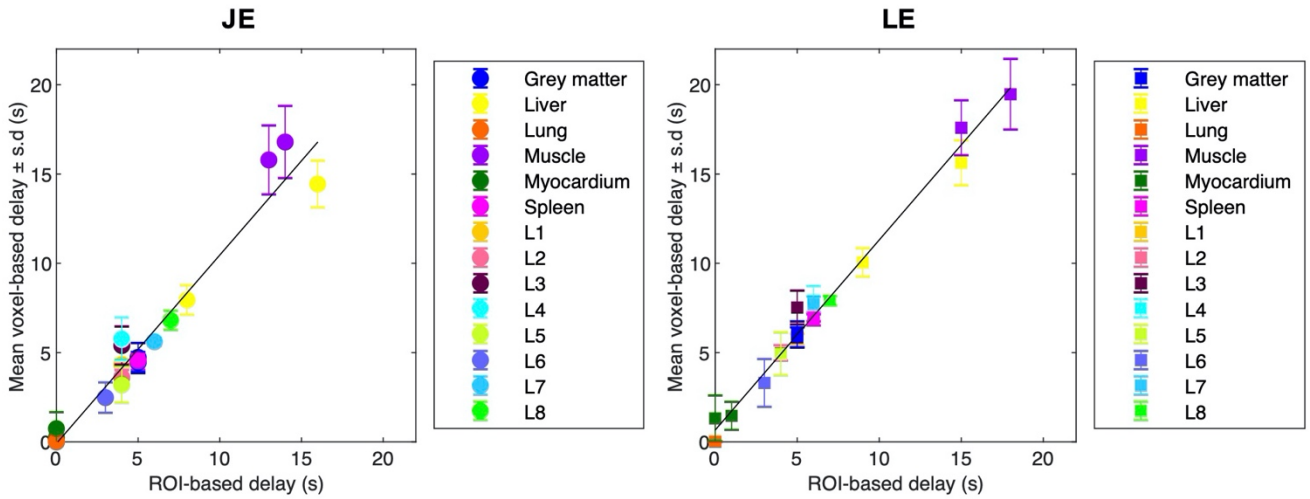

SUPPLEMENTAL FIGURE 5: Average parametric delay estimates as compared to ROI-based estimates. *Left:* JE estimates for delay (r=0.97, P<1E-3, slope: 1.05), were in strong agreement with ROI-based TAC results. *Right:* LE estimates for delay (r=0.99, P<1E-3, slope: 1.06) were also in strong agreement with ROI-based TAC results. To generate this figure, parametric delay values were averaged across all voxels per tissue. Delay estimates for both representative subjects were included.

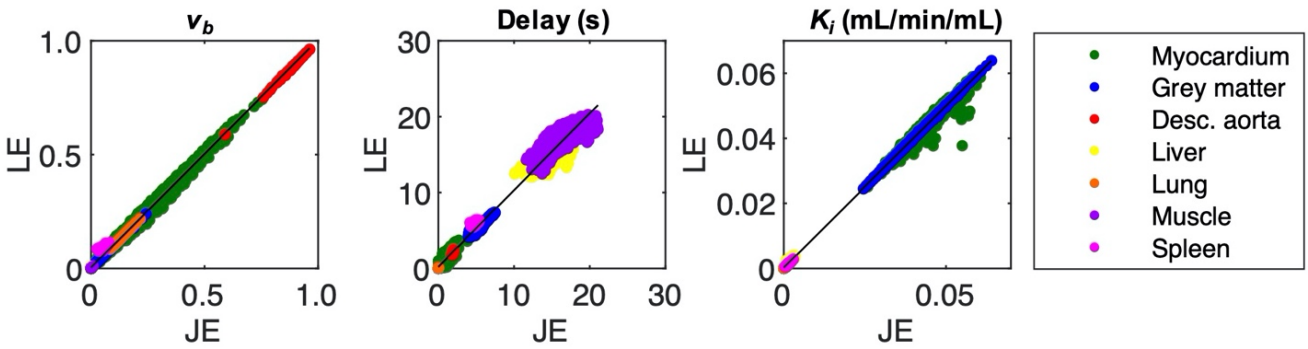

SUPPLEMENTAL FIGURE 6: Parametric LE versus JE results for a representative healthy subject. LE delay was in agreement with JE results (r=0.99, P<1E-3, slope: 1.01), but demonstrated a spread of delay values in the liver and muscle for both methods. LE estimates of v_b (r=1.00, P<1E-3, slope: 1.00) and K_i (r=1.00, P<1E-3, slope: 0.99) were in agreement with JE results.